Computational Insights into the Lattice Dynamics of Pu(IV) Oxalates

Sara B. Isbill[1*], Elodia Ciprian,[2] Jonathan H. Christian[2,3], Amy Hixon[2], Bryan J. Foley[3], Eliel Villa-Aleman[3], and Andrew J. Miskowiec[1]

[1]Oak Ridge National Laboratory, Oak Ridge, TN, 37831 USA
[2]University of Notre Dame, Notre Dame, IN, 46556 USA
[3]Savannah River National Laboratory, Aiken, SC, 29808 USA
*corresponding author: isbillsb@ornl.gov

Abstract
Despite its use in PuO_2 production, the structure of anhydrous $Pu(C_2O_4)_2$ is still not completely understood. Recently, two candidate structures for $Pu(C_2O_4)_2$ were proposed via density functional theory (DFT), after which the first experimental optical vibrational spectra were reported. Here, we calculated the lattice dynamics of the candidate structures using DFT and found that the primary difference between them is the presence of a vibrational mode near 1380 cm^{-1} in one structure. The frequency and optical activity of this mode agree well with the published experimental results, providing strong support for this calculated structure as that of anhydrous $Pu(C_2O_4)_2$.

Keywords
Plutonium, oxalates, density functional theory, phonons, Raman

Introduction

The preferred method for producing plutonium dioxide (PuO_2) in nuclear fuel reprocessing plants is through the conversion of Pu(IV) oxalate ($Pu(C_2O_4)_2$) to PuO_2 via high-temperature calcination—a process commonly referred to as the *Pu(IV) oxalate method*. This method dates back to the 1940s and is also widely used to recover Pu from waste solutions and residues.[1] Despite over 80 years of studies involving the Pu(IV) oxalate method, uncertainties still surround the exact chemical structures of species formed as $Pu(C_2O_4)_2$ thermally decomposes en route to PuO_2.[2–10] These uncertainties and more are well summarized in several reports and reviews.[9–12]

In 2021, South and Roy used density functional theory (DFT) to propose two distinct structures for anhydrous $Pu(C_2O_4)_2$.[9] Subsequently, Christian et al. performed a series of experiments to describe the breakdown of $Pu(C_2O_4)_2 \cdot 6H_2O$ during calcination en route to PuO_2.[12] Through this experimental investigation, Christian et al. heated multiple samples of hydrated Pu(IV) oxalate to various temperatures and collected detailed information on the breakdown of $Pu(C_2O_4)_2 \cdot 6H_2O$ using Raman spectroscopy, infrared (IR) spectroscopy, and powder x-ray diffraction measurements (pXRD). The spectroscopic results of this investigation are referenced below; however, the powder x-ray diffraction patterns obtained by Christian et al. were too broad

to compare directly to DFT-derived patterns, and as such, the experimental pXRD pattern of anhydrous $Pu(C_2O_4)_2$ remains elusive.

Fortunately, a compelling investigation method remains. Christian et al. reported a wealth of spectroscopic information which, in conjunction with the proposed structures published by South and Roy, provides a foundation for exploring the experimentally obtained vibrational spectra using computational methods. Recognizing the need to definitively confirm the chemical structure of $Pu(C_2O_4)_2$, we extended the work of South and Roy by calculating phonons for anhydrous $Pu(C_2O_4)_2$ based on their initial geometry optimizations. Starting from the proposed structures,[9] we calculated the phonons of two potential $Pu(C_2O_4)_2$ structures using DFT implemented via the Vienna ab initio Simulation Package (VASP 6.1)[13–15] performed on the Compute and Data Environment for Science (CADES) cluster located at Oak Ridge National Laboratory (ORNL).

South and Roy investigated the energetics of the oxalate structures, and although sufficient for their purposes, the forces were not converged tightly enough to calculate high-fidelity phonons. In the present work, the interatomic interactions were described by the exchange-correlation functional of Perdew, Burke, and Ernzerhof modified for solids (PBEsol),[16] which generally provides lattice constants in better agreement with experiment than the unmodified version.[17,18] To delocalize the electrons on Pu, the Hubbard +U correction was used with an effective U value of 6 eV on Pu and 0 eV on O and C, within the range reported by Pegg et al. for PuO_2[18,19] and consistent with the work of South and Roy.[9] Both optimizations and phonon calculations used a 450 eV cutoff energy of the plane-wave basis set, increased slightly from that used by South and Roy to account for simultaneous relaxations of unit cell volume and atomic positions.[9] A 6 × 6 × 6 k-point mesh was used for the optimizations based on the mesh used in the final single point energy calculations of South and Roy,[9] and a 3 × 3 × 3 k-point mesh was used for the phonon calculations because the phonons were calculated using a 2 × 2 × 2 supercell to reduce self-interactions within the finite displacement method implemented in Phonopy.[20] Consequently, the number of irreducible k-points in the optimizations were 80 and 108 for the oxalate-1 (**ox-1**) and oxalate-2 (**ox-2**) structures, respectively (Fig. 1), and 14 in the phonon calculations for both structures. Atomic positions of all atoms were relaxed until the forces were less than 1 meV/Å and energies for the optimization and phonon calculations were converged to less than 1×10^{-8} eV in the absence of dispersion corrections. Magnetic moments and all other parameters are consistent with the optimization inputs in South and Roy.[9]

As summarized in Table 1, the tighter value of convergence coupled with denser k-point meshes and no dispersion corrections did not significantly change the symmetry of the structure from that reported by South and Roy;[9] however, differences in the lattice vectors were noted. In particular, for **ox-1**, the *a* and *c* vectors were longer, and the *b* lattice vector was slightly shorter, whereas for **ox-2**, the *a* lattice vector was shorter, and *b* and *c* lattice vectors were longer. These differences resulted in notable changes in the volume, especially for the **ox-2** structure in which a volume 58 $Å^3$ larger than the volume in South and Roy was calculated.

The primary difference between the **ox-1** and **ox-2** structures involves the orientation of the oxalate ligands. In **ox-1**, the oxalate C–C bonds lie along the [001] direction, and the Pu atoms are collinear in the *ab* plane (Fig. 1c). In **ox-2**, the oxalate ligands are rotated relative to the [001] plane (Fig. 1b). Also, in **ox-2**, the Pu atoms are not collinear but instead form a zigzag structure with every other atom offset by ± 20° from *b* relative to its neighboring Pu atoms (Fig. 1d). Consequently, although **ox-1** has *C*2/*m* symmetry, **ox-2** has *P*1 symmetry using the default symmetry tolerance in Phonopy (1×10^{-5} $Å^{-1}$). Loosening the symmetry tolerance to 1×10^{-3} $Å^{-1}$ increases the symmetry of **ox-2** to 2/*m*.

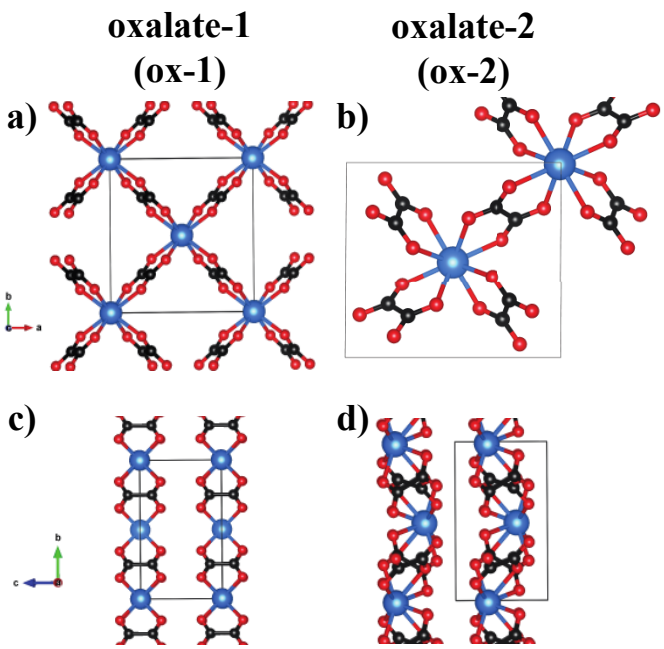

Figure 1: Optimized structures of proposed $Pu(C_2O_4)_2$ structures: (a, c) **ox-1** and (b, d) **ox-2**.

Table 1. Relaxed cell dimensions for **ox-1** and **ox-2** determined in the present work compared with those from South and Roy.[9]

Value	ox-1 (Ref. 9)	ox-1 (present)	Change	ox-2 (Ref. 9)	ox-2 (present)	Change
a (Å)	8.51	8.62	+0.11	9.19	8.75	–0.44
b (Å)	8.87	8.83	–0.04	7.07	8.14	+1.07
c (Å)	5.19	5.47	+0.28	4.28	4.71	+0.43
α (°)	90.0	90.0	0.00	90.04	89.99	–0.05
β (°)	107.1	106.9	–0.19	90.29	90.03	–0.26
γ (°)	90.0	90.0	0.00	85.51	89.86	4.35
Space group	*C*2/*m*	*C*2/*m*†	--	*P*1	*P*1†	--
Volume (Å³)	391.76	398.13	+6.37	278.08	336.13	+58.05

†Space groups with a symmetry tolerance of 1×10^{-5} Å^{-1}.

The phonons of both candidate oxalate structures were calculated to determine their stability. The band structures and phonon density of states (pDOS) for **ox-1** and **ox-2** are given in Fig. 2. Both structures show distinct bands that are relatively flat across the Brillouin zone, especially for energies above approximately 300 cm^{-1}. Notably, the **ox-1** structure has a sizeable imaginary mode (52.6 cm^{-1}) at Γ, indicating a structural instability that is absent in the **ox-2** structure. The eigenvector of the imaginary 52.6 cm^{-1} mode (Fig. 3) was visualized using VESTA[21] and reveals that the instability involves the orientation of the oxalate ligands relative to the *ab*

plane. Specifically, the mode is a rotation of the oxalate ligands that would transform **ox-1** into the **ox-2** structure, clearly showing that **ox-2** is the preferred structure of $Pu(C_2O_4)_2$ at 0 K.

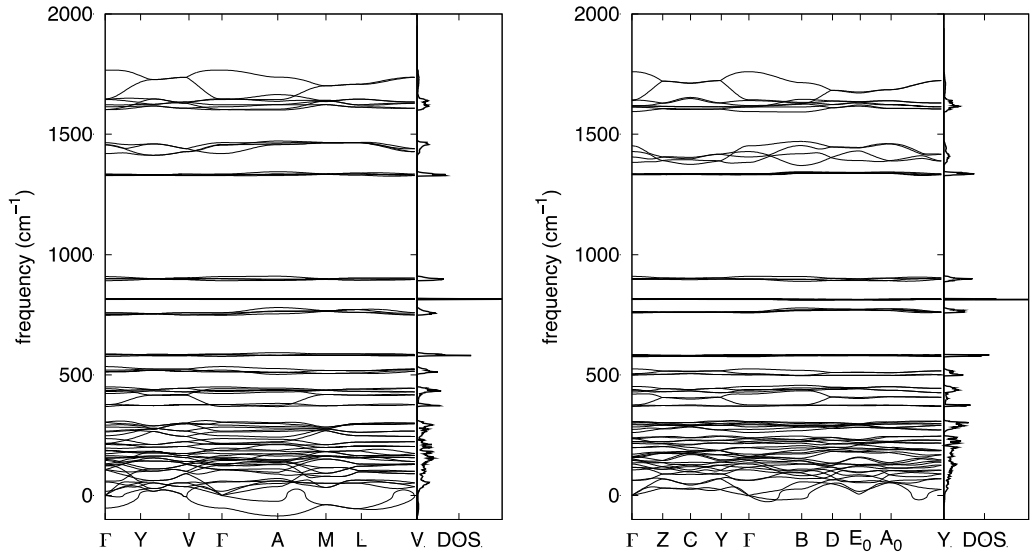

Figure 2: Band structure and pDOS of **ox-1** (left) and **ox-2** (right).

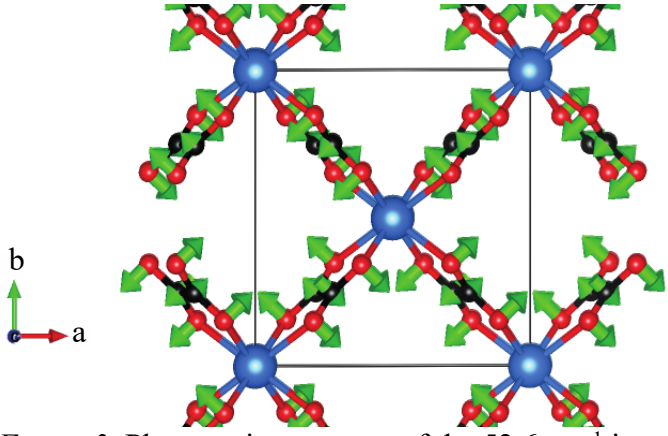

Figure 3: Phonon eigenvectors of the 52.6 cm^{-1} imaginary mode in **ox-1**.

The pDOS for **ox-1** and **ox-2** (Fig. 4) were used to identify any distinguishing differences in the lattice dynamics of the two structures that may be optically active for comparison with recent experiments at finite temperatures.[12] The most significant difference in the pDOS between **ox-1** and **ox-2** is seen around 1400–1450 cm^{-1}. In the calculated pDOS of **ox-1**, a vibrational band is centered at 1450 cm^{-1} and is 60 cm^{-1} wide . The corresponding band in **ox-2** is centered at 1420 cm^{-1} and spans 100 cm^{-1}. Inspection of the vibrational frequencies at the Γ point, the relevant region of the Brillouin zone for comparing to the spectra of Christian et al., shows that **ox-2** has a mode at 1383 cm^{-1} that involves coupled C–C and C–O stretches (Fig. 5). In this mode, the two sets of stretches on the left side of the molecule are antisymmetric with the two sets of stretches on the right side of the molecule. More specifically, as the C–C bonds on the left contract, the C–C bonds on the right are elongated. Additionally, as the C–O bonds on the left are elongated, the C–O bonds on the right contract. The same mode in **ox-1** is located at 1456 cm^{-1}. In Figures 1c and 1d, the Pu–

Pu orientation and oxalate coordination normal to the [100] plane are shown. In **ox-2**, the Pu atoms are noncollinear along the [010] axis, and every other atom lies 20° off the *b*-axis relative to its neighbor. This buckling along [010] also pulls the oxalate ligands toward +*b* or –b, breaking the degeneracy of the different mode symmetries compared with the planar **ox-1** structure.

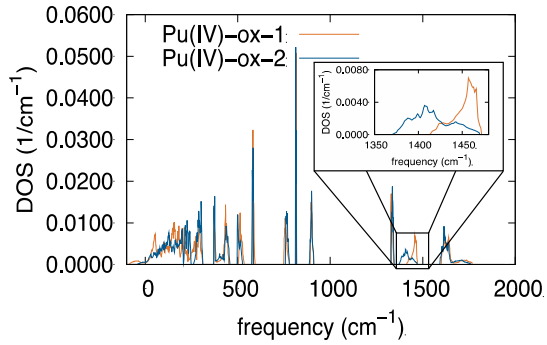

Figure 4: pDOS of the **ox-1** and **ox-2** structures generated with a 14 × 14 × 14 mesh.

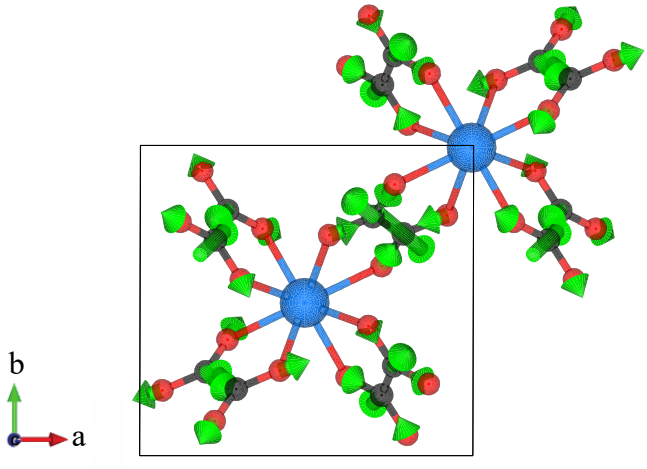

Figure 5: Phonon eigenvectors of the 1383 cm^{-1} mode in **ox-2**.

Group theory analysis revealed the space group of the **ox-2** structure to be *P*1 when using the default symmetry tolerance of Phonopy (1×10^{-5} Å^{-1}), which has only one irreducible representation that predicts all modes to be both IR and Raman active. Reducing the symmetry tolerance to 1×10^{-3} Å^{-1} increases the symmetry to 2/*m*, corresponding to the C_{2h} point group. Under this symmetry, the irreducible representation of the 1383 cm^{-1} mode is B_g and is expected to be Raman active but not IR active. Modes that are not optically active in the 2/*m* space group likely have very low intensities when they become active through small structural distortions that reduce the symmetry to *P*1. As such, this mode is expected to have nonnegligible activity in the Raman spectrum, and the IR activity is expected to be small.

The Raman and IR frequencies of Pu(IV) oxalate thermal degradation products were recently reported by Christian et al.[12] While isolation of the hygroscopic compounds $Pu(C_2O_4)_2 \cdot H_2O$ and $Pu(C_2O_4)_2$ is challenging, $Pu(C_2O_4)_2 \cdot 6H_2O$ clearly forms at low temperature,

$Pu(C_2O_4)_2•2H_2O$ is formed by partial dehydration of $Pu(C_2O_4)_2•6H_2O$ at slightly elevated temperatures, and PuO_2 is formed as the temperature increases further. Because we computationally investigated an anhydrous Pu(IV) oxalate, our results compare best with the 220 and 250 °C experimental data (i.e., **Pu-220** and **Pu-250**) reported in Christian et al. In those products, most or all of the water had likely evaporated from the material en route to PuO_2. Inspection of the experimentally measured peaks reported in Table 1 of Christian et al.[12] shows a Raman-active mode at 1382 cm^{-1} for the **Pu-220** and **Pu-250** data that was assigned to a C–O stretch. Our calculated vibrational mode at 1383 cm^{-1} involves both C–C and C–O stretches and, as previously discussed, is expected by theory to be Raman active and in excellent agreement with the experimentally measured feature. Thus, we conclude that the **ox-2** structure is likely present in the thermal degradation products of Pu(IV) oxalate. An optical vibrational feature around 1380 cm^{-1} was reported for experimental measurements at all temperatures investigated in Christian et al., but the activity changes from Raman active to IR active above 250 °C. Additional DFT calculations would be needed to provide insights into the nature of the modes at 1386 and 1362 cm^{-1} for the **Pu-350** and **Pu-450** data, respectively, because the oxalate has largely degraded at these temperatures.

Although our calculations reveal a structural instability in **ox-1**, this structure could coexist with **ox-2** in a mixed phase at finite temperature. This work did not reveal any vibrational modes that are present in **ox-1** but absent in **ox-2** which could be used to determine the presence of the **ox-1** structure. Raman and IR peak intensities could reveal further information about the presence or absence of the **ox-1** phase. However, simulating the peak intensities via DFT is computationally intensive, and these calculations are currently intractable using standard high-performance computing resources.

In conclusion, we calculated the lattice dynamics of two Pu(IV) oxalate structures previously identified as possible structures for anhydrous $Pu(C_2O_4)_2$. These calculations revealed that one structure, **ox-1**, contains a structural instability. The eigenvectors of the imaginary mode are consistent with conversion to the second structure, **ox-2**, in which the Pu oxalate sheets are buckled by 20° and the oxalate ligands are not coplanar with any lattice plane. By comparing the pDOS of the two structures, we find that the **ox-2** structure is expected to contain a Raman-active mode at 1383 cm^{-1} that is absent in **ox-1**. This mode is in excellent agreement with recent experiments that observed a Raman-active mode at 1382 cm^{-1} for $Pu(C_2O_4)_2•6H_2O$ heated to 220 or 250 °C, strongly supporting the presence of the **ox-2** structure in thermal degradation products of Pu(IV) oxalate.

Acknowledgments

This research used resources of CADES at ORNL, which is supported by the US Department of Energy's Office of Science under contract no. DE-AC05-00OR22725. Part of this work has been authored by UT-Battelle, LLC, under contract DE-AC05-00OR22725 with the US Department of Energy (DOE). Part of this work was produced by Battelle Savannah River Alliance, LLC under Contract No. 89303321CEM000080 and/or a predecessor contract with the U.S. Department of Energy. The US government retains and the publisher, by accepting the article for publication, acknowledges that the US government retains a nonexclusive, paid-up, irrevocable, worldwide license to publish or reproduce the published form of this manuscript, or allow others to do so, for US government purposes. DOE will provide public access to these results of federally sponsored research in accordance with the DOE Public Access Plan (http://energy.gov/downloads/doe-

public-access-plan). The authors would like to thank Dr. Ashley E. Shields and Dr. Erik Nykwest for helpful discussions.

References

(1) Crowder, M. L.; Pierce, R. A.; Scogin, J. H.; Daniel, W. E.; King, W. D. *Small-Scale Testing of Plutionium(IV) Oxalate Precipitation and Calcination to Plutonium Oxide to Support the MOX Feed Mission (SRNL-STI-2012-00338)*; 2012.

(2) Myser, M. N. *Thermal Decomposition of Plutionium (IV) Oxalate and Hydrofluorination of Plutonium (IV) Oxalate and Oxide*; 1956.

(3) Kartushova, R. E.; Rudenko, T. I.; Fomin, V. V. Thermal Decomposition of Tetravalent and Trivalent Plutonium Oxalates. *Sov. J. At. Energy* **1958**, *5*, 831–835.

(4) Rao, G. S.; Subramanian, M. S.; Welch, G. A. Thermal Decomposition of Plutonium Oxalates. *J. lnorg. Nucl. Chem* **1963**, *25*, 1293–1300.

(5) Glasner, A. Remarks on the Thermal Decomposition of Plutonium (IV) Oxalates. *J. Inorg. Nucl. Chem.* **1964**, *26* (8), 1475–1476. https://doi.org/10.1016/0022-1902(64)80142-1.

(6) Jenkins, I. L.; Waterman, M. J. The Thermal Decomposition of Hydrated Plutonium(IV) Oxalates. *J. Inorg. Nucl. Chem.* **1964**, *26* (1), 131–137. https://doi.org/10.1016/0022-1902(64)80239-6.

(7) Nissen, D. A. The Thermal Decomposition of Plutionium (IV) Oxalate Hexahydrate. *J. Therm. Anal.* **1980**, *18*, 99–109.

(8) Karelin, A. I.; Krot, N. N.; Kozlova, R. D.; Lobas, O. P.; Matukha, V. A. Thermal Decomposition of Np(IV) and Pu(III, IV) Oxalates. *J. Radioanal. Nucl. Chem. Artic.* **1990**, *143* (1), 241–252. https://doi.org/10.1007/BF02117565.

(9) South, C. J.; Roy, L. E. Insights into the Thermal Decomposition of Plutonium(IV) Oxalate – a DFT Study of the Intermediate Structures. *J. Nucl. Mater.* **2021**, *549*, 152864. https://doi.org/10.1016/j.jnucmat.2021.152864.

(10) Vigier, N.; Grandjean, S.; Arab-Chapelet, B.; Abraham, F. Reaction Mechanisms of the Thermal Conversion of Pu(IV) Oxalate into Plutonium Oxide. *J. Alloys Compd.* **2007**, *444–445* (SPEC. ISS.), 594–597. https://doi.org/10.1016/j.jallcom.2007.01.057.

(11) Orr, R. M.; Sims, H. E.; Taylor, R. J. A Review of Plutonium Oxalate Decomposition Reactions and Effects of Decomposition Temperature on the Surface Area of the Plutonium Dioxide Product. *J. Nucl. Mater.* **2015**, *465*, 756–773. https://doi.org/10.1016/j.jnucmat.2015.06.058.

(12) Christian, J. H.; Foley, B. J.; Ciprian, E.; Dick, D. D.; Said, M.; Darvin, J.; Hixon, A.; Villa-Aleman, E. Raman and Infrared Spectra of Plutonium (IV) Oxalate and Its Thermal Degradation Products. *J. Nucl. Mater.* **2022**, *562*, 153574. https://doi.org/10.1016/j.jnucmat.2022.153574.

(13) Kresse, G.; Hafner, J. Ab Initio Molecular Dynamics for Liquid Metals. *Phys. Rev. B* **1993**, *47* (1), 558–561. https://doi.org/10.1103/PhysRevB.47.558.

(14) Kresse, G.; Furthmüller, J. Efficient Iterative Schemes for Ab Initio Total-Energy Calculations Using a Plane-Wave Basis Set. *Phys. Rev. B* **1996**, *54* (16), 11169. https://doi.org/10.1021/acs.jpca.0c01375.

(15) Kresse, G.; Furthmüller, J. Efficiency of Ab-Initio Total Energy Calculations for Metals and Semiconductors Using a Plane-Wave Basis Set. *Comput. Mater. Sci.* **1996**, *6* (1), 15–50. https://doi.org/10.1016/0927-0256(96)00008-0.

(16) Csonka, G. I.; Perdew, J. P.; Ruzsinszky, A.; Philipsen, P. H. T.; Lebègue, S.; Paier, J.; Vydrov, O. A.; Ángyán, J. G. Assessing the Performance of Recent Density Functionals for Bulk Solids. *Phys. Rev. B* **2009**, *79*, 155107. https://doi.org/10.1103/PhysRevB.79.155107.
(17) Perdew, J. P.; Burke, K.; Ernzerhof, M. Generalized Gradient Approximation Made Simple. *Phys. Rev. Lett.* **1996**, *77* (18), 3865–3868. https://doi.org/10.1103/PhysRevLett.77.3865.
(18) Pegg, J. T.; Aparicio-Anglès, X.; Storr, M.; de Leeuw, N. H. DFT+U Study of the Structures and Properties of the Actinide Dioxides. *J. Nucl. Mater.* **2017**, *492*, 269–278. https://doi.org/10.1016/j.jnucmat.2017.05.025.
(19) Pegg, J. T.; Shields, A. E.; Storr, M. T.; Wills, A. S.; Scanlon, D. O.; De Leeuw, N. H. Hidden Magnetic Order in Plutonium Dioxide Nuclear Fuel. *Phys. Chem. Chem. Phys.* **2018**, *20* (32), 20943–20951. https://doi.org/10.1039/c8cp03583k.
(20) Togo, A.; Chaput, L.; Tanaka, I. Distributions of Phonon Lifetimes in Brillouin Zones. *Phys. Rev. B* **2015**, *91* (9), 094306. https://doi.org/10.1103/PhysRevB.91.094306.
(21) Momma, K.; Izumi, F. VESTA 3 for Three-Dimensional Visualization of Crystal, Volumetric and Morphology Data. *J. Appl. Crystallogr.* **2011**, *44* (6), 1272–1276. https://doi.org/10.1107/S0021889811038970.